PROCEEDINGS OF SPIE

SPIEDigitalLibrary.org/conference-proceedings-of-spie

Multi-physics simulations of label-free optical-electrical forces acting on a silica nanoparticle trapped in a SANE plasmonic nanopore

Asadzadeh, Homayoun, Renkes, Scott, Kim, Min Jun, Alexandrakis, George

Homayoun Asadzadeh Sr., Scott Renkes, Min Jun Kim, George Alexandrakis, "Multi-physics simulations of label-free optical-electrical forces acting on a silica nanoparticle trapped in a SANE plasmonic nanopore," Proc. SPIE 11978, Plasmonics in Biology and Medicine XIX, 1197803 (3 March 2022); doi: 10.1117/12.2607769

SPIE.

Event: SPIE BiOS, 2022, San Francisco, California, United States

Multi-Physics Simulations of Label-Free Optical-Electrical Forces Acting on a Silica Nanoparticle Trapped in a SANE Plasmonic Nanopore

Homayoun Asadzadeh[1], Scott Renkes[1], MinJun Kim[2] and George Alexandrakis[1,*]

[1]University of Texas at Arlington, Bioengineering Department, Arlington, TX 76010, USA
[2]Southern Methodist University, Department of Mechanical Engineering, Dallas, TX 75275, USA
[*]Corresponding author: galex@uta.edu

ABSTRACT

This work presents Multiphysics COMSOL simulations that help dissect the relative contributions of multiple forces of optical and electrical origin acting on a 20 nm diameter silica nanoparticle trapped by a plasmonic nanopore sensor. Specifically, the nanosensor uses the principle of self-induced back action (SIBA) to trap nanoparticle optically at the center of a double nanohole (DNH) structure integrated on top of a solid-state nanopores (ssNP). This novel SIBA actuated nanopore electrophoresis (SANE) sensor allows simultaneous recording of optical and electrical data features that are generated by the interaction of multiple underlying forces: Plasmonic optical trapping, electroosmosis, electrophoresis, viscous drag and heat conduction forces are all felt by a silica nanoparticle trapped by the sensor. This work aims to simulate these underlying forces in order to help understand how they contribute to the optical-electrical measurements generated by sensor. Furthermore, experimental measurements of 20 nm silica nanoparticles trapped the SANE sensor were compared against computational predictions to test the qualitatively trends seen in experimentally measured signal profiles during the nanoparticle's approach to the optical trap and its translocation through the plasmonic nanopore, located immediately below the optical trap.

Keywords: solid-state nanopores, double nanohole, plasmonic, optical trapping, electrophoresis, electroosmosis, computational model, COMSOL

1.INTRODUCTION

Nanoapertures, fabricated in metallic films facilitate optical trapping of dielectric particles (<100 nm diameter), by utilizing the increase in optical transmission due to changes in local electric field at low beam intensities. This nanoaperture-based optical trapping approach is called self-induced back action (SIBA) [1]. Due to conservation of momentum versus diffusion forces near the nanoaperture, a photon-mediated feedback force is actuated in SIBA when a dielectric nanoparticle has a slightly different refractive index than its surrounding medium. The resulting light coupling to the far field in the dielectric nanoparticle results in increased light transmission through the plasmonic nanoaperture and therefore enables label-free detection [2]. This method has been shown to enable characterization of single proteins [3-4] and their interactions with other small biomolecules [2, 5-8].

A popular alternative for label-free detection and investigation of biomolecules at the single-molecule level employs solid-state nanopores (ssNP) [9]. Briefly, molecules which translocate through a small pore in a thin membrane are electrically detected as they go through the pore, one after another, because they temporarily alter the ionic conductance of the pore during each translocation event [10-14]. A rich literature in nanopore fabrication [15], experimental protocol implementation [16] and data analysis exists (12). Nanopore sensing has been proven useful for many applications, such as molecular size discrimination [19], investigation of biomolecular interactions [17] and investigation of local structures along elongated molecules, such as a protein bound to a DNA strand (8).

To improve quantification of bimolecular interactions, some investigators have combined nanopore sensing with plasmonic optical nanosensing. Although in some cases the additional optical measurements are only intended to augment the diversity of data types collected synchronously [18], some investigators have proposed using light power as a means of slowing down the translocation of molecules in order to increase the signal-to-noise ratio (SNR) of

Plasmonics in Biology and Medicine XIX, edited by Tuan Vo-Dinh, Ho-Pui A. Ho, Krishanu Ray,
Proc. of SPIE Vol. 11978, 1197803 · © 2022 SPIE · 1605-7422 · doi: 10.1117/12.2607769

electrical nanopore signals. Examples of such approaches have involved tweezing of a DNA-tethered micrometer bead [19] and the optical excitation of fluorescently labeled analytes to reduce their speed by manipulating the surface charge, in combination with the effects of electroosmotic flow [20]. Bowtie-shaped nanoantennas [21-27] in gold (Au) were also created to enable plasmonic enhancement of the optical field over the nanopore, which resulted in localized heating due to increased ionic conductance that did not reduce, but rather increased the analyte translocation velocity thus suggesting a compromise between throughput speed and measurement SNR.

To improve the SNR of optical-electrical measurements we have previously reported a plasmonic nanopore geometry with a double nanohole (DNH) milled through an Au layer that was deposited over a Si_3N_4 bridge structure, supported by an etched silicon wafer, with a nanopore milled at the center of the DNH structure [28]. SIBA-actuated nanopore electrophoresis (SANE) was reported as a novel sensing method, where the highest plasmonic energy is concentrated the between the DNH tips, resulting in trapping of nanoparticles and biomolecules due to dielectric loading just above the nanopore entry [29]. The advantages of the SANE sensor structure are that (a) it enables optical-electrical measurements during optical trapping for multi-second durations, before translocation through the nanopore, (b) the DNH structure in Au is known to effectively dissipate heat with minimal temperature increase at optical trapping powers [6], and (c) the electrical voltage bias drives molecules into the optical trap thus allowing measurements at ultra-low concentrations, resulting in significantly increased bound fractions between interacting molecules (30).

These interesting prior findings do not however provide any detailed insights into the relative contributions of competing optical and electrical forces that determine the experimentally observed nanopore translocation profiles. The purpose of this work was to conduct extensive Multiphysics COMSOL simulations to help dissect the relative contributions of the multiple forces acting on a 20 nm silica (SiO_2) nanoparticle trapped by the SANE sensor: The plasmonic optical trapping force, electroosmosis, electrophoresis, viscous drag and heat conduction inducing convection currents. Furthermore, experimental measurements of 20 nm SiO_2 nanoparticles trapped at the sensor were compared against computational predictions to test the qualitatively trends seen in the experimentally measured signal profiles during the nanoparticle's approach to the optical trap and its translocation through the plasmonic nanopore.

2. MATERIALS AND COMPUTATIONAL METHODS

2.1 SANE Sensor Geometry and Computational Parameters

The nanofabrication procedures for the SANE sensor, the detailed optical-electrical experimental measurement setup, the trapping and translocation measurements for 20 nm SiO_2 nanoparticles, and data analysis methods have all been reported previously [31]. Only a few points relevant to the simulations performed in this work will be repeated here. The simulated SANE sensor geometry is shown in Fig. 1. The COMSOL simulations assumed the geometry of a DNH formed in Au, drilled into the physical sensor by Ne ion focused ion beam (FIB) milling (CNMS, Oak Ridge National Laboratory, Oak Ridge, TN). FIB endpoint detection during milling enabled stopping the process when the underlying Si_3N_4 layer was reached and a 25 nm pore was milled through the Si_3N_4 layer, at the center of the DNH, with He ion FIB. The Au-Si_3N_4 layers at the center of the sensor area were suspended as a bridge prior to FIB milling through successive chemical etching steps that removed the underlying material layers one by one, while front-side and back-side photomasks guided the precise alignment of the etching patterns, as described previously [32]. Only the central area of the sensor geometry, delineated by a green dashed line in Fig. 1(c) was included in the COMSOL simulations performed in this work. All other areas were assumed to be too far to affect computational results**.** Table 1 lists the SANE sensor layer geometry thicknesses and the optical and electrical properties of materials in each sensor layer assumed in the simulations. Table 2 lists all relevant physical parameters assumed for the external laser illumination, voltage bias and analytes, reflecting the same parameters used in the physical experiments for 20 nm SiO_2 nanoparticles, as described previously [33]:

Material	Thickness (nm)	Optical properties (Refractive index)	Electrical Properties	
			Dielectric constant	Conductivity
Gold	100	1.33	6.9	45.6E6[S/m]
Si_3N_4	50	1.8	9.5	Negligible

Table 1. Optical and electrical properties assumed for the sensor's Au and Si_3N_4 layers.

Description	Expression
Surface charge density of Si_3N_4	-0.02 [C/ m^2]
Surface charge density of Au	0 [C/ m^2]
Th concentration of KCl	1 [mol·dm^{-3}]
K+ diffusion coefficient	1.96e-9 [$m^2 \cdot s^{-1}$]
Cl- diffusion coefficient	2.03e-9 [$m^2 \cdot s^{-1}$]
Valence of K +	1
Valence of CL -	-1
Laser power	5-11 [mW]
Voltage bias	100-400 [mV]
Temperature	300 [K]
Relative Permittivity of Electrolyte	80
Permittivity of Vacuum	8.85×10^{-12} [F/m]
Viscosity of solution	10^{-3} [Pa.s]
pH	7.4
Wavelength	830 [nm]
Space charge density of KCL	96485e3 [C/mol]

Table 2. Physical and chemical parameters assumed in the COMSOL computations performed in this work.

Once a nanoparticle is inside the optical trap it couples light into the far field, which increases light transmission through the SANE sensor, while the nanoparticle's physical presence in the nanopore creates current blockage that is detected as a transient decrease in conductance [34]. COMSOL simulations were performed for a 20 nm SiO2 nanoparticle translocating through the midline of the SANE sensor. In order to compute the ionic current, an integral was taken from the all-ion current flow which is passing along the DNH/ssNP (green dashed line, fig.1-c), and for computing the optical transmission all angles of the lights were collected and computed bellow the ssNP.

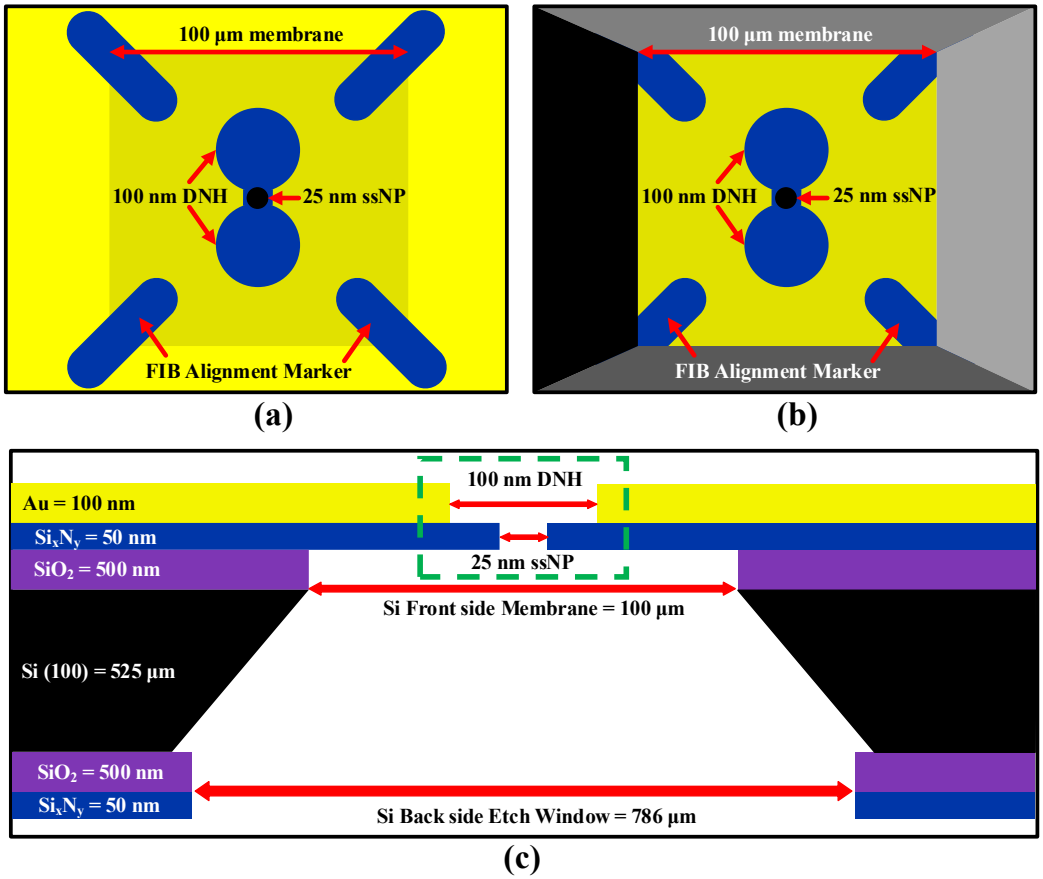

Figure 1. (a) Frontside view of SANE chip. (b) Backside view of SANE chip. (c) Cross-section of the SANE sensor chip. The green-dashed rectangle in (c) indicates the COMSOL simulation domain.

2.2 Governing Equations for the Optical-Electrical Fields in the Simulated Volume of the SANE Sensor

The physics of ionic liquids can be approximated by three coupled classical equations: the Poisson equation relevant to electrostatics, the Nernst-Planck equation (NPE) describing ionic-flux, and the Navier-Stokes equation (NSE) governing the fluid flow. The Poisson equation (PE), which implement the electrostatic field in the Au and Si_3N_4 layers of the sensor, relates the electric potential V to the charge distribution ρv, and is given by:

$$\nabla^2 V = -\frac{\rho v}{\epsilon_0 \epsilon_r} \tag{2-1}$$

where $\epsilon_0 \sim$ 8.85e-12 F/m is the permittivity of free space and ϵ_r is the relative permittivity, inherent property of the material and ρv is volume charge density. The charge distribution (volume charge density) can relate the electrostatic field with the ionic concentration and space charge density which will be effective in forming the electric Debye layer (EDL) on the nanopore's wall in the SANE sensor. The related charge density equation can be represented in terms of the ionic concentrations as:

$$\rho v = N_A e \sum z_i c_i \tag{2-2}$$

where $N_A \sim 6{\times}1023\ mol^{-1}$ is the Avogadro's constant, $e \sim$ 1.6e-19 C represented the elementary charge, z_i is the valence number and c_i is the molar concentration of species i in the electrolyte. Monovalent electrolytes have been used in the majority of nanopore-based studies [35]. In the present study, 1M Potassium Chloride (KCl) has been assumed as the electrolyte and the pH was set at 7.4.

The space charge density of this salt, because of its binary and monovalent nature, can be expressed as:

$$\rho v = N_A e[C_{k+} - C_{Cl-}] \quad (2\text{-}3)$$

The flux J_i for each ionic species i is calculated using the Nernst-Planck equation:

$$J_i = -D_i \nabla_{ci} - Z\left(\frac{D_i}{RT}\right) F C_i \nabla V + u c_i \quad (2\text{-}4)$$

Looking at the equation closely, it may be deduced that the overall ionic flux is influenced by three components. The first part is caused by a concentration gradient [36], as described by Fick's first law of diffusion. The ionic flux generated by the formation of an electric field is the second part, and the advection of ionic species by the fluid velocity field is the third component. The first and third components are the most important contributors to ionic flux in the case of the SANE senor because they cause the diffusion and convection of the ionic species in the electrolyte (KCl), Both of these components are coupled to the second component of electrokinetic flow (migration in electric field). The related module in the COMSOL will be discussed in the next section.

The continuity and momentum (Navier-Stokes) equations can be used to define a Newtonian fluid in an isothermal condition and by coupling these equations with the computational fluid dynamic (CFD) technique in the entire computational domain of the SANE sensor the fluid motion can be simulated. Also, the Reynolds number Re = ρvL/μ is a dimensionless quantity which distinguishes the laminar from turbulent flow regime, where v and L are the flow velocity and length scale of the nanopore in the sensor (~160nm). In the present study, since fluid velocity is very low, Re is estimated to be ~ 0.0001, placing these simulations is in the laminar flow regime. Also, because the advective term in the Navier-Stokes equation can be neglected when viscous forces are greater than inertial forces, which are negligible here, and under steady conditions for fluid flow, we have a simplified momentum equation valid for low Re values, known as 'Creeping flow [37]:

$$\nabla^2 u = -\nabla P \quad (2\text{-}5)$$

The electrokinetic transport inside the nanopores is governed by the combination of equations 2-1, 2-4, and 2-5.

To compute the light field distribution created by light focused onto the Maxwell's equations (ME) will be solved, and is given by:

$$\nabla \times {\mu_r}^{-1}(\nabla \times E) - {k_0}^2\left(\varepsilon_r - \frac{j\sigma}{\omega\varepsilon_0}\right) E = 0 \quad (2\text{-}6)$$

where E is the electric field amplitude, ε_0 the permittivity of vacuum, j the current density, ω the angular frequency, σ the electrical conductivity, μ_r the relative permeability of the material and ε_r is the relative permittivity.

The final equation is the convection heat transfer which is derived from energy equation and for the steady-state domain and can be represented by this heat equation (HE):

$$\rho C_p u.\nabla T + (\nabla.q) += Q \quad (2\text{-}7)$$

where ρ is the fluid density, C_p is the specific thermal capacity, u is the fluid velocity, q is the heat flux by conduction and Q is the heat source. Combination of equations (2-6) and (2-7) will govern the temperature field created at the sensor by light beam illumination.

2.3 Forces on a dielectric nanoparticle

2.3.1 Drag Force

Under low Re flow regimes (creeping flow), the viscous drag force on a spherical target (the nanoparticle in our studies) can be expressed as:

$$F_{Di} = -6\pi\eta r v \quad (2\text{-}8)$$

where η is viscosity of the medium, r the effective radius of the particle and v is the velocity of motion in the fluid.

2.3.2 Electrophoretic Force

Having the net electric field (equation 3-1), the electrostatic force exerted on a charged ion particle is computed by [38]:

$$F = ez_pE_i \tag{2-9}$$

2.3.3 Dielectrophoretic Force

The target particle can become polarized and induce a dipole moment in the presence of a spatially non-homogeneous electric field. As a result, a suspended particle can be pushed under such a field regardless of its surface charge by the Dielectrophoretic (DEP) force [39]:

$$F_{DEP} = 2\pi r^3 \varepsilon_m \alpha \nabla E^2 \tag{2-10}$$

where r is the particle radius, ε_m the medium permittivity, and α is the Clausius-Mossotti factor represented by:

$$\alpha = \frac{\sigma_p - \sigma_m}{\sigma_p + 2\sigma_m} \tag{2-11}$$

where σ_p and σ_m are the complex permittivity of the particle and the medium, respectively. The DEP force exerted on a particle will push it towards either the stronger or the weaker field areas, depending on whether the sign is positive or negative. Since in the present study the α is equal to +0.5, the DEP force always pushes the nanoparticle to the region with stronger electric field, from *cis* to *trans.*

2.3.4 Electroosmotic Force

The electrolyte cationic species will move closer to the pore surface if there is a net negative surface charge density (σ) in the nanopore wall and an external electric field be applied. This positive-charge heavy surface suspended in the electrolyte gives boost to a fluid flow. As soon as the voltage bias is applied, the cations are drawn towards the cathode (negatively charged electrode). This retarding force manifests as a retarding hydrodynamic force, which will add to the intrinsic viscosity of the fluid. This is known as the Electroosmotic force (F_{EOF}) and is a function of Debye length emerging away from the charged pore wall surface. Because of the double layer developed on the pore surface, the electroosmotic mobility of the fluid may be reported as a function of the zeta potential, which can be calculated using equation (2-12):

$$\mu_{EOF} = -\left(\frac{\varepsilon \zeta_{pore}}{\eta}\right) \tag{2-12}$$

where ε is the relative permittivity of the medium and ζ is the zeta-potential of the walls of the nanopore. Graham's equation can be applied to approximate the zeta-potential in the above equation [40], which relates ζ to the estimated surface charge density of the nanopore. For the present work it was evaluated to be -0.02 C/m^2 [41].

Using the Helmholtz–Smoluchowski equation, the electroosmotic velocity can be represented as:

$$u_{EOF} = (E.\mu_{EOF}) \tag{2-13}$$

Finally, the electroosmotic force (F_{EOF}) evaluated using equation (2-14):

$$F_{EOF} = m.\frac{d(u_{EOF})}{dt} \tag{2-14}$$

where m represented the fluid mass in each grid of computational domain's finite element meshes.

2.3.5 Thermophoretic Force

The thermophoretic force is exerted on a particle as a result of temperature variations in the background fluid. The thermophoretic force is defined as:

$$F_{tp} = \frac{6\pi d_p \mu^2 C_s \Lambda \nabla T}{\rho(2\Lambda+1)T} \tag{2-15}$$

where k is the thermal conductivity of the fluid, k_p is the particle thermal conductivity, T the fluid temperature, and C_s is a dimensionless constant equal to 1.17 and Λ=k_f/k_p which represent the thermal conductivity of the fluid and nanoparticle, respectively [42].

2.3.6 Light Force

The potential energy of the particle in the optical trap created by the concentration of plasmonic field intensity at the center of the DNH is defined by:

$$U = \frac{1}{2}\alpha|E^2| \tag{2-16}$$

where E represents the light field amplitude and α is the real part of complex permittivity, represented by:

$$\alpha = \frac{\varepsilon^* p - \varepsilon^* m}{\varepsilon^* p + 2\varepsilon^* m} \tag{2-17}$$

where $\varepsilon^* p$ and $\varepsilon^* m$ are the complex permittivity of the particle and the medium, respectively. The complex permittivity is expressed by $\varepsilon^* = \varepsilon - (j\sigma/\omega)$, where ε is the real permittivity, σ the conductivity, and ω is the angular frequency of the applied electric field. For a 20 nm SiO_2 dielectric nanoparticle, the imaginary part of the permittivity is negligible, and the real part of the permittivity is ~1.1.

Then the light force can be defined as [43]:

$$F = -\frac{dU}{dt} \tag{2-18}$$

2.3.7 Brownian Force

Collisions of continuous-phase fluid molecules with a particle produce the Brownian force on that particle. In submicron dimensions, Brownian motion of particles can become important. [44]. The Brownian force is treated as a Gaussian white noise random process [45] with spectral intensity along all computational domains in this study, and can be represented as follows:

$$F = \xi\sqrt{\frac{12\pi\mu T r_p k_B}{\Delta t}} \tag{2-19}$$

where k_B = 1.3806488 e−23 J/K is the Boltzmann constant, r_p is the particle radius, Δt the time step that used by the solver, μ the fluid dynamic viscosity, T the absolute fluid temperature and ξ is a normally distributed random number with a mean of zero and unit standard deviation.

2.3 Finite Element Modeling of Electrical-Optical Force Fields in COMSOL

The impact of the above-described forces and their interactions on a 20 nm SiO2 nanoparticle was simulated by COMSOL Multiphysics (version 5.6, Natick, MA), approximating as closely as possible the parameters of physical experiments. The 2D simulation domain was composed of two reservoirs of ionic liquid with two connecting structures in-between (DNH gap in the Au layer and the ssNP in the Si_3N_4 layer), both 25 nm across, as shown in Fig. 1(a).

The simulation began with the NPE computing the dynamics of ions in the electrolyte, attained by the transport of diluted species module. The PE was then used to describe the electric field distribution throughout the simulation volume using the electrostatics module. The NSE was used to define the movement of water, realized by the laminar flow module. The ME was used to describe the light field distribution, attained by the wave optic module and the HE computed the temperature field using the heat transfer module.

In Fig. 1(a) the electrolyte domains (blue) the NPE, PE, and NSE were fully coupled and applied in a self-consistent way. In the Si_3N_4 domain (gray), representing the nanopore membrane, the PE was applied to describe the electric field distribution and was coupled to the NPE and NSE. In the Au domain (yellow) the ME and HE were fully coupled. Also, for computing the forces on the nanoparticle the NPE, HE, NSE and PE were fully coupled.

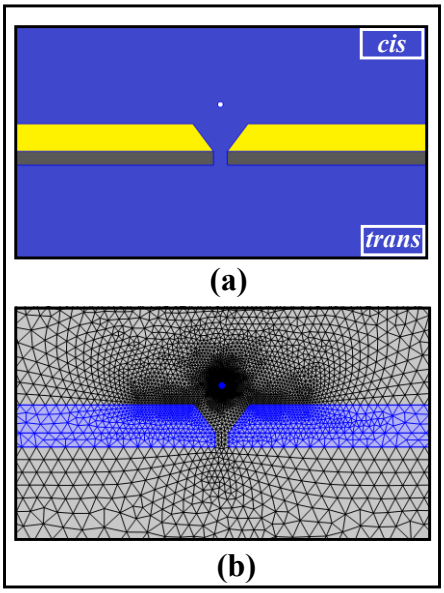

Figure 2. The computational domain of the SANE sensor. (a) The geometry in which yellow, gray, blue and white indicates the Au layer with the DNH gap, grey indicates the Si_3N_4 layer with the ssNP, and blue and white indicate electrolyte reservoirs and the nanoparticle, respectively. (b) The mesh elements in the computational domain span a broad range of sizes with a finer mesh around the nanoparticle, sharp corners and around the nanopore volume.

For the boundary condition, in the electrostatic module for solving the PE, a surface charge density for the nanopore wall and nanoparticle surface were created (Table 2) and an electrical potential and ground was assigned at the top and bottom borders respectively (*cis* and *trans*). Also, the space charge density was assigned for the KCl domain. In the laminar flow module, the normal flow (P= 0 Pa) was considered for the top and bottom surfaces as a boundary condition in solving the NSE [46]. On all other solid boundaries, a no-slip velocity boundary condition was adopted for solving the NSE. The electroosmotic velocity boundary condition was applied for the nanopore wall in order to compute the electroosmotic velocity field. A volume force was created by 'space charge' × 'electric field' assigned to the KCl domains. For the transport of dilute species module, the initial concentrations on the boundaries of 1 M KCl for the *trans* and *cis* sides were assigned to solve the NPEs, and zero (normal) electromigration and diffusion flux at all other solid boundaries [47]. Also the 'Convection' and 'Migration in Electric Field' were selected for the transport mechanisms in the laminar flow module. The diffusion coefficient and the concentration of each ion, i.e., K+, Cl-, were created and assigned in the transport of diluted species module (Table 2).

In the wave optic module for solving the ME, a perfectly matched layer was used at the top and bottom surfaces to avoid back-scattering at the outer boundaries and perfect electrical conductor was assumed for side boundaries of the Au layer. For heat transfer module to compute the HE, thermal convection in all surrounded boundaries and thermal

sources around the Au layer were applied as boundary conditions. Quadratic triangular elements were used in the finite element calculations.

Because the precision of numerical solutions is highly influenced by mesh size, a refined mesh was required in the region near the surface where the dependent variables' gradients are prominent. In this study, 'Physics Controlled Mesh' was chosen with the size 'Finer' in the mesh generation part of software to capture the small variations in potential, ionic concentration, and velocity near the charged membrane surface, as shown in Fig. 1(b). It should be noted that the maximum element size far from the DNH was set to 1/10 of the light wavelength (830 nm) to solve the ME [48]. Finally, the stationary option for solving the NPE, HE, NSE, and PE and a frequency domain option for solving the ME were assigned.

One limitation of the COMSOL package was that, in the present study one cannot couple the wave optic and transport of dilute species so, ME was not coupled to all other forces. Therefore, it was not possible to let the nanoparticle propagate through the nanopore against the optical trapping force in a time-dependent simulation. Instead, the resultant of all forces was computed for different vertical positions along the midline of the nanopore and then by using the Newton's second law in equation (2-20) along the vertical path in the DNH/ssNP the translocation time of the nanoparticle was computed:

$$\sum F = m.a \tag{2-20}$$

It should be mentioned that the relative velocity between the particle and fluid in the aforementioned equation were computed and updated in the 1000 steps, by a cod that was written in the MATLAB [37].

3-RESULTS

Figure 3(a) presents a typical experimental measurement of a multi-second trapping event by the SANE sensor for a single 20 nm SiO_2 nanoparticle. A step increase in transmitted light intensity is seen upon trapping in Fig. 3(b) and a step decrease upon leaving the trap in Fig. 3(c).

The dielectric loading of the trap by the 20 nm nanoparticle resulted in a ~10% increase in optical transmission through the DNH (Particle entry; Fig. 3(a)). Simultaneously, a high-frequency transient was observed in the raw ionic current (Fig. 4(a)), with a maximum positive current computed at 44 pA, which was ~19 times greater than the baseline nanopore current. Also, axial nanoparticle oscillations that we refer to as 'bobbing' likely occurred during optical trapping, just over nanopore's entrance. These oscillations created ionic current fluctuations while the nanoparticle was optically for a few seconds These fluctuation measurements have no equivalent in classic nanopore measurements.

The nanoparticle was seen bobbing intermittently inside the DNH trap for around 2.15 seconds (Fig. 4 (a), green dashed line). Subsequently a characteristic negative ionic current pulse due to nanopore blockage was observed at the end of the capturing cycle, while the nanoparticle translocated across the ssNP from the *cis* to *trans* (Fig. 4(a), blue dashed line). This electrical spike coincided in time with the optical transmission reduction event (Fig. 3(a), blue dashed line).

In order to test the validity of the computational method, experimental results were compared to the simulation output. To this end, the optical transmission and ionic current, which are key data types generated by the SANE senor were computed. The magnified image of the optical transmission for the particle entry and particle exit are presented in Figs. 3(b) and 3(c), respectively. As the results show, the experimental translocation time for the particle entry and particle exit states is of the order of few μs (Figs. 3(b) and 3(c)). On the other hand, in the numerical simulation, the optical transmission versus translocation time was computed for different nanoparticle locations, and location was translated to time using Newton's second law (equation (2-20), Figs. 3(d) and 3(e)). In Fig. 3(d), once the negatively charged nanoparticle enters the DNH, the optical transmission is increased to similar levels to the ones observed experimentally. However, the approximation used for describing particle velocity based on the COMSOL-calculated forces is clearly inadequate as it predicts translocation times of ~100 μs which are much too long compared to the experimental results (Fig. 3(b)). Similarly, once the negatively charged nanoparticle exits the ssNP, the optical transmission is declines back to baseline, but the discrepancy between experimentally the observed translocation time

of few μs (Fig. 3(c)) and the calculated one of ~160 μs (Fig. 3(e)) remains. In near future work we will revisit this discrepancy to clarify and address its sources.

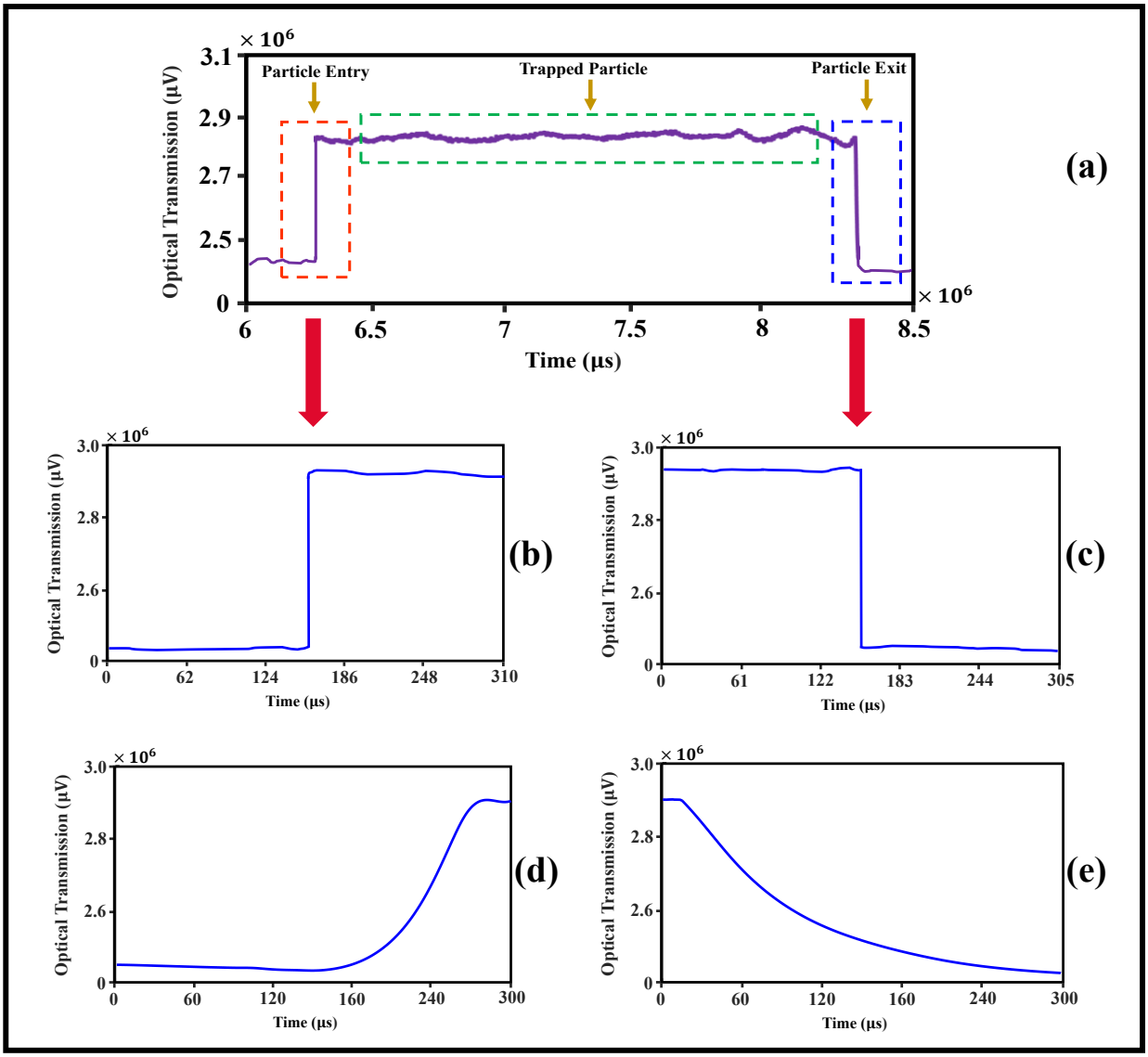

Figure 3. (a) Plot of experimentally measured optical transmission intensity versus time for the 20 nm SiO2 nanoparticle entering the optical trap (red dashed line), staying in the trap (green dashed line) and exiting the trap (blue dashed line) and magnified the of optical transmission change upon trap entrance (b) and exit (c). Computational results for the relative change in transmitted light intensity versus time upon trap entrance (d) and exit (e) for the simulated SiO2 nanoparticle.

Furthermore, the electrical measurement results were compared to the simulation outcome. The magnified image of the electrical measurement for particle entry and particle exit are presented in Figs. 4(b) and 4(c), respectively. As these figures show, the translocation time for the particle entry and particle exit states are 320 and 324 μs respectively. The corresponding computational results for the ionic current are depicted in Figs. 4(d) and 4(e). Comparison of these figures shows, when the 20 nm nanoparticle is trapped by the DNH (Particle entry), a spike increase in the ionic current occurs with a maximum current peak at 49 pA. Consequently, when the nanoparticle is released from the ssNP a spike decrease in the ionic current occurs at -47 pA, respectively. The computational and experimental measurements

in this case appear qualitatively consistent. Also, as can be seen in Fig. 4(a) one spike is positive, meaning the current flows from *trans* to *cis*, which is not seen in the traditional nanopores. It should be mentioned that the electrical spike profiles are similarly asymmetric in both computational and experimental results.

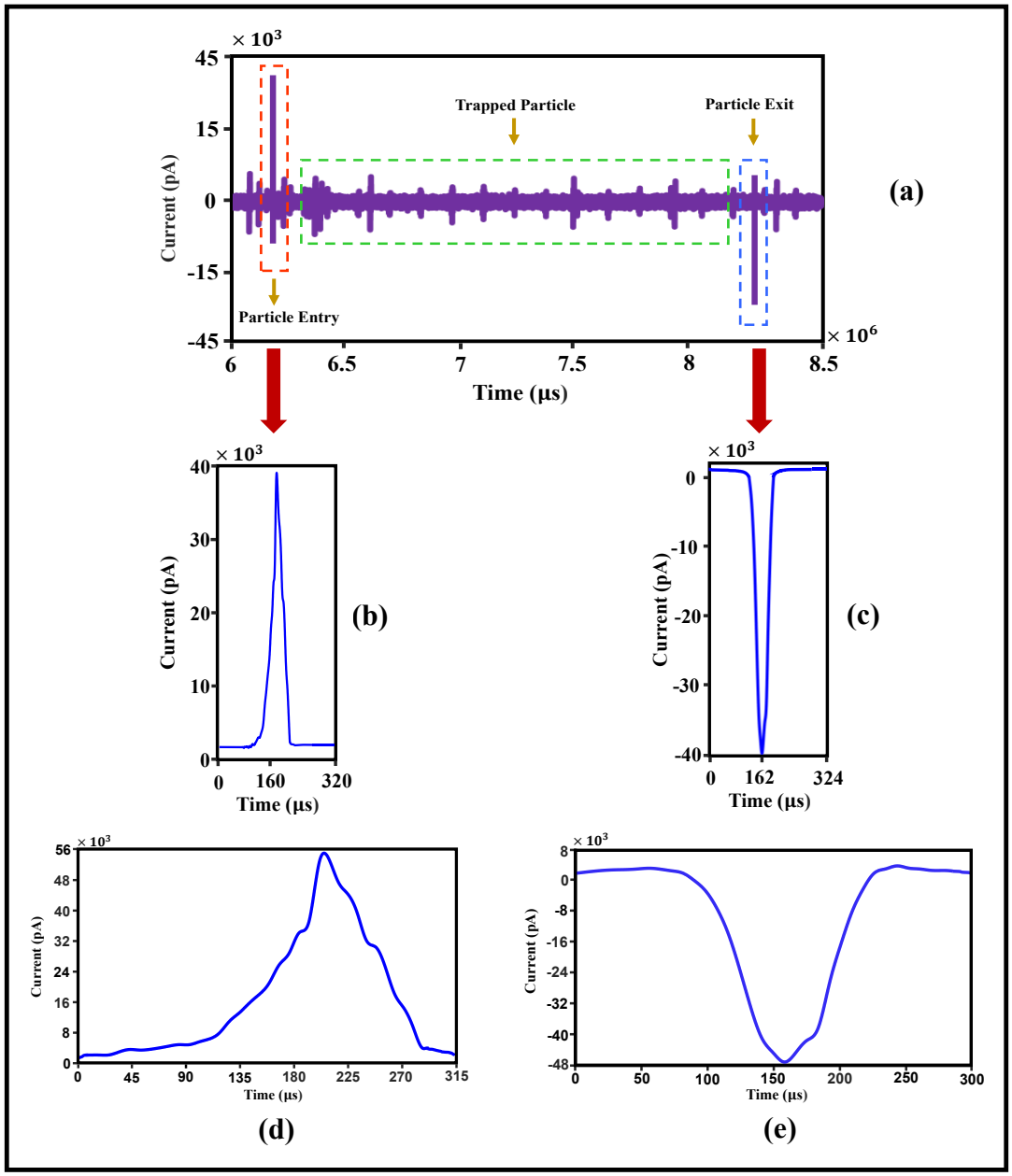

Figure 4. Plots of ionic current versus time for the particle entry (red dashed lines), trapped particle (green dashed lines), and particle exit (blue dashed lines) (a). Magnified images of ionic current at particle entry (b) and exit (c) can be compared qualitatively related to experimental results with corresponding computational results in (d) and (e).

3.1. Computation of Spatial Variation in Physical Parameters with Axial Nanoparticle Position in the Sensor

An advantage of simulations is that they can help provide estimates, and even spatially resolved maps, of physical quantities that are not easily accessible experimentally. Here, COMSOL simulations were used to estimate the values of several key physical parameters that affect the trajectory of the nanoparticle through the SANE sensor. Namely, these are the electrostatic field strength, light intensity, KCl analyte velocity and temperature fields. By solving equation (2-1) and equation (2-6) the electrostatic field distribution due to the externally applied bias and the light field amplitude distribution at 830 nm and various laser powers were computed, respectively, and their values were plotted as a function of nanoparticle axial location along the SANE sensor. Figure 5(a) shows, the maximum electric field acting on the nanoparticle as a function of axial position through the sensor, with the zero distance (x = 0 nm in all figures) being set at the interface between the Au and Si_3N_4 layers. The maximum electric field value occurred just before the negatively charged nanoparticle reached that DNH/ssNP border (x~ -12 nm). At a similar axial location (x~ -14 nm), the light electric field also reached a maximum due to plasmonic focusing near the sharp corners of the DNH structure (Fig. 5(b)). Figures 5(a) and 5(b) also indicate that increases in voltage bias or incident light power, resulted in increases in the corresponding electric field amplitudes acting on the nanoparticle.

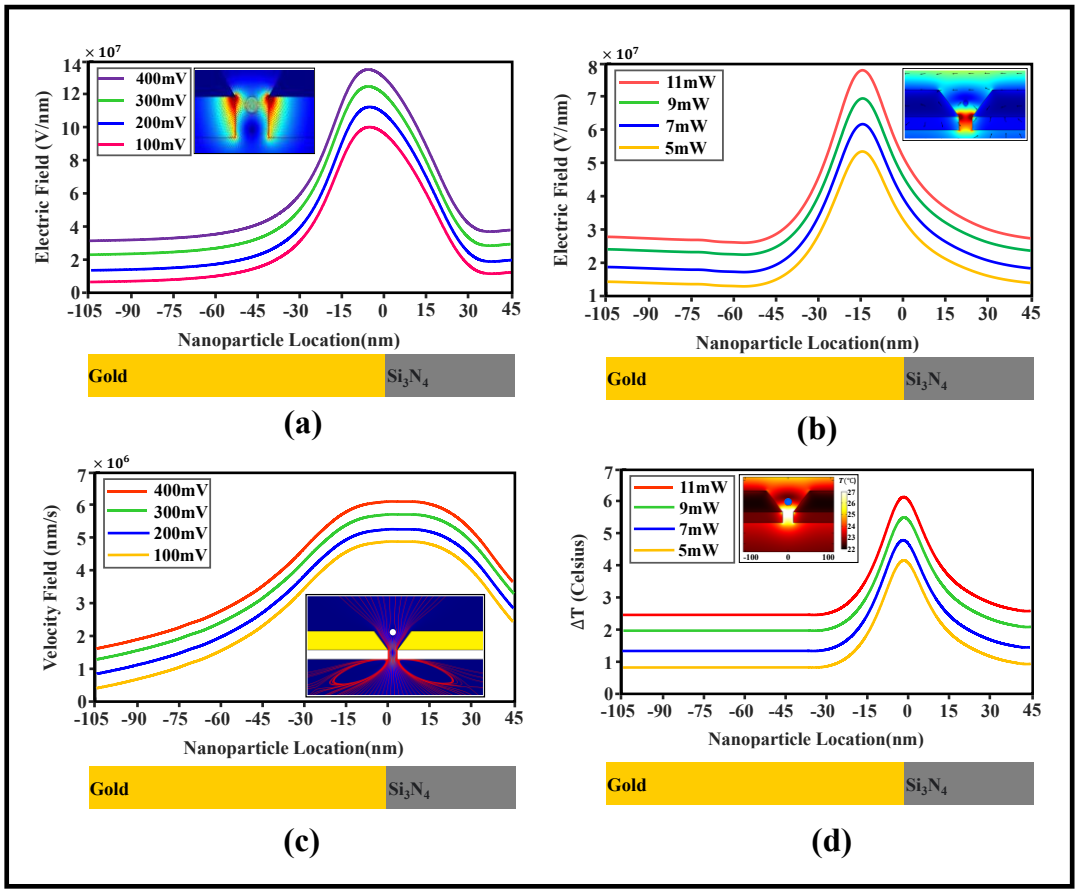

Figure 5. (a) Electrostatic field amplitude, (b) light field amplitude, (c) ionic fluid velocity field, (c) and temperature field for four different external voltage bias values as a function of axial location inside the sensor for the 20 nm SiO2 nanoparticle. The yellow and gray color bars represent the Au and Si_3N_4 regions, respectively. The figure insets provide sample views of the spatial distribution of each of these parameters for a specific nanoparticle location. Insets in (a), (b) and (d) are color maps with brighter colors indicating higher values, and (c) shows contours of constant fluid speed along with its streamlines.

In contrast to the voltage bias and electric field profiles that peaked just above the DNH/ssNP interface, analyte fluid velocity and temperature increases due to localized heating both reached maximum values at that interface (x= 0 nm). By solving equations (2-1) and (2-5) the magnitude of the velocity field induced by the electrophoretic effect was obtained, while any rise in voltage bias induced increased fluid flow velocity accordingly (Fig. 5(c)). A rise in fluid velocity was expected intuitively, based on Bernoulli's principle, to be at the x= 0 nm location as fluid rushes from

the more open DNH region into the narrower nanopore channel. Finally, by integrating and solving equations (2-6) and (2-7), the temperature field was computed. The maximum temperature also occurred near the x= 0 nm plasmonic focusing regions, due to high values of light field intensity that was partly converted to Joule heating.

3.2 Computation of Spatial Variation in Forces on the Nanoparticle with Axial Position in the Sensor

By solving equation (2-9) one can obtain the electrophoretic force as a function of axial nanoparticle location for different external voltage bias levels (Fig. 6(a)). The maximum electrophoretic force occurred close to where the electrostatic field reached its peak values (x= -12 nm). The sign of the electrophoretic force indicated that it pushed down on the negatively charged nanoparticle from *cis* to *trans* and that any rise in voltage bias would also increase the magnitude of this force. By solving equation (2-10), one can obtain the dielectrophoretic force for different voltage biases as a function of nanoparticle axial location (Fig. 6(b)). The maximum dielectrophoretic force occurred at the region with the highest electric field value (x= -12 nm; as in Fig. 6(a)) and increased with increasing voltage bias. It is worth mentioning that EP forces are dependent on both the electric field and electrical charge of nanoparticles [37], while the DEP force is dependent on the electric field and the polarizability of nanoparticles. Since α in equation (2-11) is positive, the DEP force will push the nanoparticle toward the strongest field (from *cis* to *trans*, in this case). In the nanopore wall regions positive electrical charge was present because of the EDL. Thus, the polarizability of the nanoparticle increased, which consequently increased the DEP force.

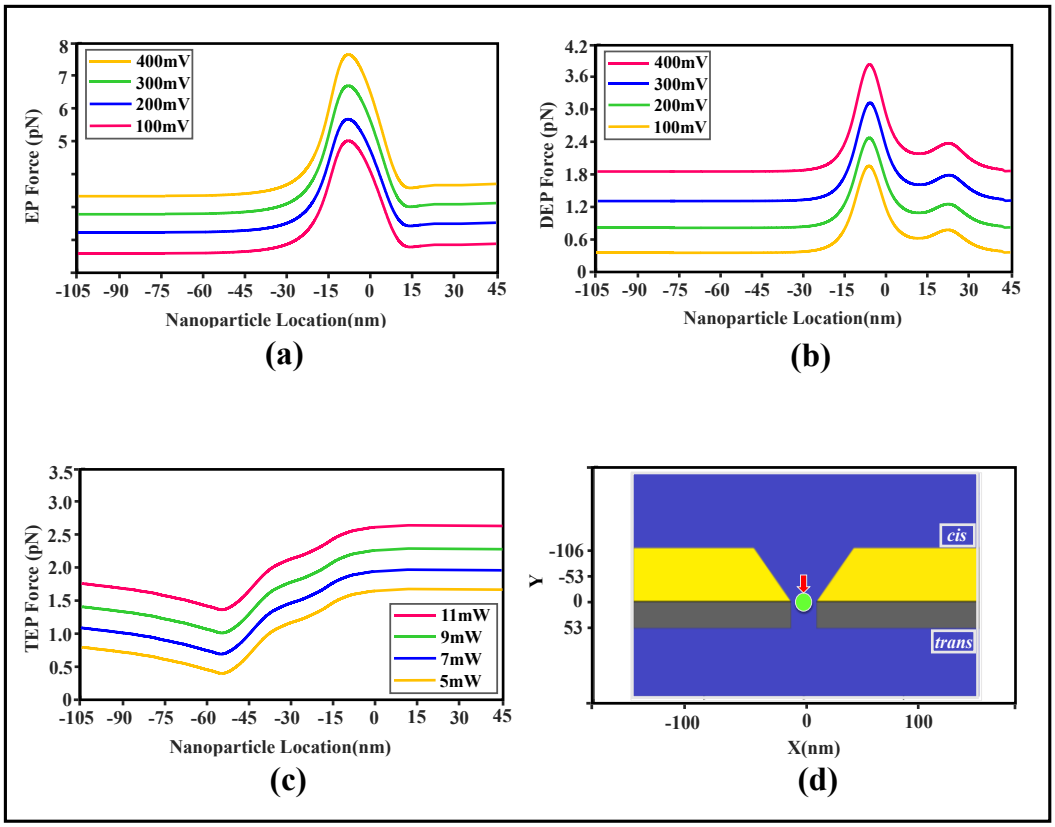

Figure 6. Plots of the electrophoretic (a), dielectrophoretic (b), and thermophoretic (c) forces as a function of nanoparticle axial location and voltage bias. (d) Sensor geometry indicating spatial dimensions along the axial (X) and longitudinal dimension (Y) with the red arrow indicating the directionality of all three forces from *cis* to *trans*

Finally, by solving equation (2-15), the thermophoretic (TEP) force was obtained for various laser powers as a function of axial nanoparticle location. These calculations indicated that the maximum TEP force occurred just above the DNH/ssNP border where the maximum plasmonically-localized light intensity and heating exists (Fig. 6(c)). This force pushed nanoparticles from *cis* to

trans. Figure 6(d) provides a reference for the nanoparticle locations relative to the DNH/ssNP border (x= 0 nm) and indicates that all of the EP, DEP and TEP forces pushed the nanoparticle in the same direction.

The viscous drag force is one of the two components in slowing down molecule translocations and by solving equation (2-8) one can compute this force for various nanoparticle locations and external voltage biases (Fig.7(a)). The maximum drag force occurred where the electrostatic field and consequently the velocity magnitude have their maximum values [49]. It can be observed that the drag force pushed the negatively charged nanoparticle from *trans* to *cis* because the drag force always opposed the velocity vector. Also, an increase in the voltage bias increased the magnitude of this force [37]. The optical trapping force can be obtained by solving equation (2-18) for different laser powers and nanoparticle locations (Fig.7(b)). The maximum trapping force occurred at regions with the highest light field intensity values, near the DNH/ssNP border, where plasmonic enhancement was maximum, and increased with increasing laser power. The optical trapping force pushed the nanoparticle from *trans* to *cis*, opposing translocation through the SANE sensor. Lastly, by solving equation (2-14), one can compute the electroosmotic force for various nanoparticle locations and voltage bias levels (Fig. 7(c)). In the electroosmotic phenomenon, a net negative surface charge density on the nanopore wall coupled with the external electric field to move the electrolyte cationic species closer to the pore's surface. This positive-charge heavy planar surface suspended in the electrolyte gave rise to a fluid flow and drove the fluid toward the anode electrode. Thus, in the present study, the electroosmotic force tended to push the nanoparticle from *trans* to *cis.* Importantly, the electroosmotic force was assumed to not occur in the at DNH layer because the surface charge density of Au was zero, assuming a perfect conductor, and a Debye layer would not form there. Figure 7(d) provides a reference for the nanoparticle locations relative to the DNH/ssNP border (x= 0 nm) and indicates that all of the viscous drag, optical trapping and electroosmotic forces pushed the nanoparticle in the same direction, which opposed translocation through the sensor.

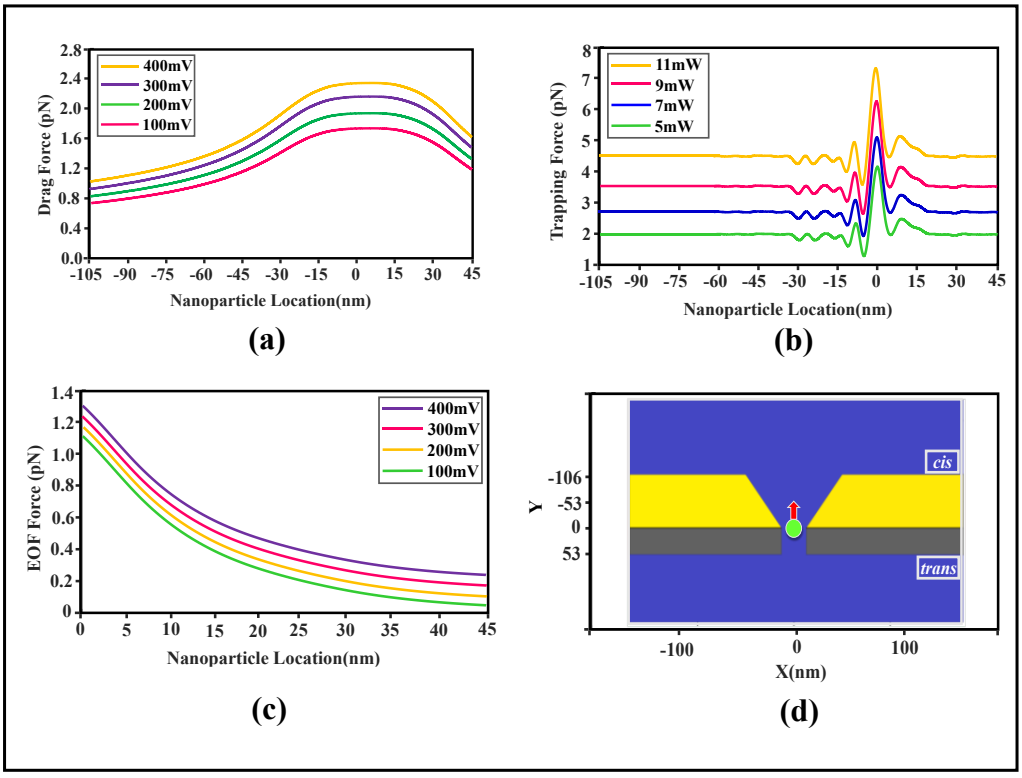

Figure 7. Plots of the viscous drag (a), optical trapping (b), and electroosmotic (c) forces as a function of nanoparticle axial location and voltage bias. (d) Sensor geometry indicating spatial dimensions along the axial (X) and longitudinal dimension (Y) with the red arrow indicating the directionality of all three forces from *trans* to *cis*.

In Table 3 the maximum value of each of the COMSOL-simulated forces known to act on the nanoparticle in the SANE sensor are listed. In this Table, the forces are divided into two parts; forces which pushed the nanoparticle from

cis to *trans* (EP, DEP and TEP) and ones that pushed it from *trans* to *cis* (TR, EOF and Viscous Drag). The EP, DEP, EOF and Viscous Drag were computed for the 100mV external voltge bias and the TEP and TR forces were computed for 5 mW laser power, to match experimental conditions. These calculations indicated that the strongest force acting on the nanoarticle is the EP, while the smallest size force was the Brownian one (equation 2-19).

Type of Forces	Symbol	Direction	Voltage/laser power	Maximum Value (pN)
Electrophoretic	F_{EP}	*cis* to *trans*	100mV	3.99
Dielectrophoretic	F_{DEP}	*cis* to *trans*	100mV	1.4
Thermophoretic	F_{TEP}	*cis* to *trans*	5 mW	1.2
Trapping	F_{TR}	*trans* to *cis*	5 mW	-3.88
Drag	F_D	*trans* to *cis*	100mV	-1.7
Electroosmotic	F_{EOF}	*trans* to *cis*	100mV	-1.29
Brownian	F_{BR}	Any direction	——	1.5×10^{-2}

Table 3. Maximum value and directionality of each of the forces known to act on a 20 nm SiO_2 nanoprticle in the SANE sensor.

One of the most important computation outcomes of Table 3 is that the values of the optical trapping and electrophoretic forces are very similar and act in opposite direcions, consistent with stable nanoparticle trapping. It should also be mentioned that, the gravitational force would also contribute to pushing the nanoparticle from *cis* to *trans* but its magnitude for the 20 nm nanoparticle is about 2e-3 (pN), which is negligible.

DISCUSSION AND CONCLUSION

The purpose of this work was to simulate by COMSOL Multiphysics the optical and electrical forces acting on a 20 nm SiO_2 nanoparticle trapped inside the SANE sensor. Given that it would be challenging to measure experimentally all of those forces and their spatial distributions, the simulations were used to help dissect the relative contribution of each of these forces to the total force acting on the nanoparticle for different axial locations throughout the sensor.

Firstly, the step-increase/decrease in optical transmission when the nanoparticle entered/exited the optical trapped by the DNH and the simultaneous transient increase/decrease in current conduction through the underlying nanopore, respectively, were simulated. Although all the equations describing the influence of the externally applied volage bias on to the sensor, the KCl ionic liquid, and the dielectric nanoparticle could be solved fully coupled in COMSOL, this software package did not offer coupling with Maxwell's equations. Therefore, the optical forces and the heating gradient near the regions where plasmonic focusing was the highest, could not be coupled to the forces of electrical origin. As a result, the time-dependent dynamics of the nanoparticle through the sensor could not be computed directly. Instead, in this work the optical trapping (Fig. 3) and electrical translocation (Fig. 4) profiles were computed for a range of static axial positions of the nanoparticle throughout the sensor. An simple and approximate physical model involving Newton' second law was implemented to compute the nanoparticle's instantaneous velocities at different locations through the sensor, which were in turn used to map axial position to time. The simulations matched qualitatively the amplitudes of relative optical signal change to experimentally measured ones (Figs. 3(b) – 3(e)) but predicted much slower translocation times compared to experiments. In contrast, qualitatively similar profiles were attained between computation and experiment for current spike amplitude and translocation time. Interestingly, the

simulations also reproduced the temporal asymmetry seen in experimentally measured current spikes (Figs. 4(b) – 4(e)).

In the next step, the simulations were used to compute the spatial variation of key physical parameters as a function of axial position along the SANE sensor. The simulation results indicated that both the electric field due to the external voltage bias as well as the electric field of light illumination peaked above the DNH/ssNP interface. This is interpreted to be an effect of the sharp corners of the Au material at the narrowest point of the DNH. This plasmonic field focusing implies that, in contrast to bare nanopores, the nanoparticle was acted on by a strong external voltage bias pushing it forward even before it reached the nanopores' mouth. However, with the light source switched on, the concentrated light field opposed this movement towards the nanopore's mouth. The triangular shape of the DNH also affected the ionic fluid velocity profile through the sensor (Fig. 3(c)). The narrowing near the top side of the nanopore created a Bernoulli effect that increased ionic fluid velocity driven by electrophoresis at zero pressure differential between the *cis* and *trans* reservoirs. Electroosmotic and thermophoretic forces also contributed to opposing or enhancing, respectively, the forward fluid movement, as discussed below. However, these results show that electrophoresis was the dominant force near the nanopore, which resulted in increased fluid velocity above the DNH/ssNP interface. Lastly, the change in temperature due to plasmonic light absorption also was highest near the DNH/ssNP interface even though the highest amount of heating occurred a few nm above, presumably because of the geometric asymmetry of the DNH that allowed for more rapid cooling from the top side of the interface.

Subsequent computations focused on the spatial variation in forces exerted on the nanoparticle as a function of its axial position along the SANE sensor. Simulation results were grouped by forces promoting nanoparticle translocation versus ones opposing it. Of the forces promoting translocation electrophoresis was the strongest. Comparison on Fig. 3(a) to Fig. 4(a) suggests that the electrophoretic force's relative strength was highest at the same location where the external voltage bias was maximum. Dielectrophoretic forces exist due to electric field gradients, and for this SANE sensor geometry the steepest gradient occurred just before the entrance and just before the exit (secondary peak) of the ssNP (Fig. 4(b)). The thermophoretic force was understandably more spatially distributed as heat diffusion and convection tended to reduce the steepness of the temperature gradient created near the sharp corners of the DNH. On the other hand, of the forces opposing translocation, the optical one was the strongest. Interestingly, the light wave interference patterns created a strong and spatially narrow force maximum near the DNH/ssNP interface, where the nanoparticle was likely trapped the longest, as well as secondary maxima on either side (Fig. 7(b)). The secondary maxima in the optical force profile suggest that the nanoparticle would encounter opposition to translocation even before reaching the main peak in optical trapping force. The viscous drag opposition force on the other hand (Fig. 7(a)), though smaller in amplitude than the optical force, was more spatially extended profile that mirrored that of the ionic fluid velocity (Fig. 5(c)). Lastly, the electroosmotic force was the smallest of opposing forces in relative size and was considered to be non-zero over the walls of the ssNP, as the Au material of the DNH above it was considered to be an ideal conductor. In practice, the Au surface could also form a Debye layer due to a pH-dependent proton adsorption of oxide species from solution [49].

In conclusion, the simulations performed in this work demonstrated that the dominant force near the sensor is the electrophoretic one, while at the center of the sensor the optical force is maximal, as expected for achieving trapping. The simulations also indicated the relative contributions of a number of additional forces that enhanced or opposed particle translocation as a function of axial position along the sensor. Computation of all force profiles is instructive for the selection of experimental conditions to manipulate those forces in future work. These simulations showed that the sum total of the optical force, electroosmotic force and viscous drag are only barely larger than the sum total of the electrophoretic, dielectrophoretic and thermophoretic forces. One can therefore imagine that some external perturbation could interrupt optical trapping. However, the source of that external perturbation is not clear currently. The simulation indicated that the nanoparticle's escape from the optical trap is unlikely to be facilitated by Brownian motion, as this force appeared to be very small. There are other effects that could interrupt nanoparticle trapping that are unaccounted for in the simulations but are present in physical experiments. For example, laser source power fluctuations and applied voltage bias fluctuations may momentarily add up to facilitate nanoparticle escape. In

addition, in physical experiments several nanoparticles can accumulate over the sensor's trapping volume, being pushed there by the applied bias. It is possible that one of these approaching particles could knock onto the particle already inside the optical trap and initiate bobbing motions, or even induce particle escape [50]. Finally, it is important to mention that the results presented in this work are only approximate, not only because of the aforementioned COMSOL limitation for coupling Maxwell's equations to the transport of diluted species and electrostatic modules, but also because this solver assumes continuum equations that do not take into account effects that become important at the nanoscale [51]. Nevertheless, simulations can help augment the qualitative understanding of forces at play in this plasmonic nanopore sensor, which can help interpretation of signals from biomolecules obtained with this sensor in future work.

ACKNOWLEDGMENTS

We thank Dr. Karren L. More and Dr. Alex Belianinov for allowing us access and providing technical guidance on focused ion beam milling at the Center for Nanophase Materials Sciences (CNMS) at Oak Ridge National Laboratory (ORNL) in Oak Ridge, TN. We are also thankful to all the engineers and staff at the Shimadzu Institute Nanotechnology Research Center at the University of Texas at Arlington for their support and guidance. The authors acknowledge the financial support from the National Cancer Institute (1R21CA240220-01A1), the National Heart, Lung, and Blood Institute (NIH T32 HL134613) for Scott Renkes and the National Science Foundation (CBET#2022398 and CBET#2022374). The content is solely the responsibility of the authors and does not necessarily represent the official views of the National Institutes of Health.

References

1. Ashkin, "History of optical trapping and manipulation of small-neutral particle, atoms, and molecules," IEEE Journal of Selected Topics in Quantum Electronics, 6 (6), 841 –856 (2000).
2. A. A. Al Balushi, A. Kotnala, S. Wheaton, "Label-free free-solution nanoaperture optical tweezers for single molecule protein studies," Analyst, 140 (14), 4760 –4778 (2015).
3. M. L. Juan, R. Gordon, Y. Pang, "Self-induced back-action optical trapping of dielectric nanoparticles," Nature Physics, 5 (12), 915 (2009).
4. A. A. Al Balushi, A. Zehtabi-Oskuie, and R. Gordon, "Observing single protein binding by optical transmission through a double nanohole aperture in a metal film," Biomedical optics express, 4 (9), 1504 – 1511 (2013).
5. Y. Pang, and R. Gordon, "Optical trapping of a single protein," Nano letters, 12 (1), 402 –406 (2011).
6. S. Wheaton, and R. Gordon, "Molecular weight characterization of single globular proteins using optical nanotweezers," Analyst, 140 (14), 4799 –4803 (2015).
7. A. A. Al Balushi, and R. Gordon, "Label-Free Free Solution Single Protein-Small Molecule Binding Kinetics: An Optical Tweezer Approach.,"
8. A. A. Al Balushi, and R. Gordon, "A label-free untethered approach to single-molecule protein binding kinetics," Nano letters, 14 (10), 5787 –5791 (2014).
9. A. A. Al Balushi, and R. Gordon, "Label-free free-solution single-molecule protein–small molecule interaction observed by double-nanohole plasmonic trapping," ACS Photonics, 1 (5), 389 –393 (2014).
10. A. A. Balushi, and R. Gordon, "Dynamic Variation in Protein-Small Molecule Interaction Observed by Double-Nanohole Optical Trapping,"
11. A. Kotnala, D. DePaoli, and R. Gordon, "Sensing nanoparticles using a double nanohole optical trap," Lab on a Chip, 13 (20), 4142 –4146 (2013).
12. L. Kumar, A. Lesuffleur, M. Hughes, "Double nanohole apex-enhanced transmission in metal films," Applied Physics B, 84 (1-2), 25 (2006).
13. Y. Pang, and R. Gordon, "Optical trapping of 12 nm dielectric spheres using double-nanoholes in a gold film," Nano letters, 11 (9), 3763 –3767 (2011).
14. D. W. Deamer, and M. Akeson, "Nanopores and nucleic acids: prospects for ultrarapid sequencing," Trends in biotechnology, 18 (4), 147 –151 (2000).

15. J. J. Kasianowicz, E. Brandin, D. Branton, “Characterization of individual polynucleotide molecules using a membrane channel,” Proceedings of the National Academy of Sciences, 93 (24), 13770 –13773 (1996).
16. B. M. Venkatesan, and R. Bashir, “Nanopore sensors for nucleic acid analysis,” Nature nanotechnology, 6 (10), 615 (2011).
17. U. F. Keyser, “Controlling molecular transport through nanopores,” Journal of The Royal Society Interface, 8 (63), 1369 –1378 (2011).
18. Y. Feng, Y. Zhang, C. Ying, “Nanopore-based fourth-generation DNA sequencing technology,” Genomics, proteomics & bioinformatics, 13 (1), 4 –16 (2015).
19. S. W. Kowalczyk, T. R. Blosser, and C. Dekker, “Biomimetic nanopores: learning from and about nature,” Trends in biotechnology, 29 (12), 607 –614 (2011).
20. L. Ma, and S. L. Cockroft, “Biological Nanopores for Single-Molecule Biophysics,” ChemBioChem, 11 (1), 2534 (2010).
21. C. Dekker, “Solid-state nanopores,” Nature nanotechnology, 2 (4), 209 (2007).
22. B. N. Miles, A. P. Ivanov, K. A. Wilson, “Single molecule sensing with solid-state nanopores: novel materials, methods, and applications,” Chemical Society Reviews, 42 (1), 15 –28 (2013).
23. A. Storm, J. Chen, X. Ling, “Fabrication of solid-state nanopores with single-nanometre precision,” Nature materials, 2 (8), 537 (2003).
24. W. Shi, A. K. Friedman, and L. A. Baker, “Nanopore sensing,” Analytical chemistry, 89 (1), 157 –188 (2016).
25. Z. Yuan, C. Wang, X. Yi, “Solid-State Nanopore,” Nanoscale research letters, 13 (1), 56 (2018).
26. G. F. Schneider, S. W. Kowalczyk, V. E. Calado, “DNA translocation through graphene nanopores,” Nano letters, 10 (8), 3163 –3167 (2010).
27. C. Plesa, and C. Dekker, “Data analysis methods for solid-state nanopores,” Nanotechnology, 26 (8), 084003 (2015).
28. M. U. Raza, S. S. S. Peri, L.C. Ma, S.M. Iqbal and G. Alexandrakis,” Self-induced back action actuated nanopore electrophoresis (SANE)” Nanotechnology, 29 ,435501 (10pp), (2018).
29. D. Fologea, B. Ledden, D. S. McNabb, “Electrical characterization of protein molecules by a solid-state nanopore,” Applied physics letters, 91 (5), 053901 (2007).
30. R. M. Smeets, U. F. Keyser, D. Krapf, “Salt dependence of ion transport and DNA translocation through solid-state nanopores,” Nano letters, 6 (1), 89 –95 (2006).
31. S. S. S. Peri, M. K Sabnani, M. U. Raza, S. Ghaffari, S. Gimlin, D. D. Wawro, J. S. Lee, M. J. Kim, J. Weidanz and G. Alexandrakis,” Detection of specific antibody-ligand interactions with a self-induced back-action actuated nanopore electrophoresis, Nanotechnology, 31, 085502, (2020).
32. T. Z. Butler, M. Pavlenok, I. M. Derrington, “Single-molecule DNA detection with an engineered MspA protein nanopore,” Proceedings of the National Academy of Sciences, 105 (52), 20647 –20652 (2008)
33. K. J. Freedman, A. R. Bastian, I. Chaiken, “Solid-state nanopore detection of protein complexes: applications in healthcare and protein kinetics,” Small, 9 (5), 750 –759 (2013)
34. B. N. Miles, A. P. Ivanov, K. A. Wilson, “Single molecule sensing with solid-state nanopores: novel materials, methods, and applications,” Chemical Society Reviews, 42 (1), 15 –28 (2013).
35. N. Razmjooei, Y. H. Ko, F. A. Simlan, and R. Magnusson, “Resonant reflection by microsphere arrays with AR-quenched Mie scattering,” Optics express, 29(12), 19183-19192 (2021).
36. A. Storm, J. Chen, X. Ling, “Fabrication of solid-state nanopores with single-nanometre precision,” Nature materials, 2 (8), 537 (2003).
37. S. Jahromi, E. Amani and S. Movahed,” An improved hybrid continuum-atomistic four-way coupled model for electrokinetics in nanofluidics,” Electrophoresis, 40(12), 1678-1690 (2019).
38. W. Shi, A. K. Friedman, and L. A. Baker, “Nanopore sensing,” Analytical chemistry, 89 (1), 157 –188 (2016).
39. H.Asadzadeh, A.Moosavi, G. Alexandrakis and M. RK. Mofrad,” Atomic Scale Interactions between RNA and DNA Aptamers with the TNF-α Protein,” BioMed Research International, (2021).
40. H.Asadzadeh, A. Moosavi, A. Etemadi,” Numerical simulation of drag reduction in microgrooved substrates using lattice-Boltzmann method,”Journal of fluid engineering, 141(7),(2019).
41. Z. Yuan, C. Wang, X. Yi, “Solid-State Nanopore,” Nanoscale research letters, 13 (1), 56 (2018).
42. Y.H. Ko, N. Razmjooei, H. Hemmati and R. Magnusson, “Perfectly-reflecting guided-mode-resonant photonic lattices possessing Mie modal memory,” Optics express, 29(17), 26971-26982 (2021)

43. G. F. Schneider, S. W. Kowalczyk, V. E. Calado, “DNA translocation through graphene nanopores,” Nano letters, 10 (8), 3163 –3167 (2010).
44. Sindhu Preetham Burugupally, Bhargav Koppolu, Negar Danesh, Yongkuk Lee, Vidisha Indeewari, Bin Li. Enhancing the performance of dielectric elastomer actuators through the approach of distributed electrode array with fractal interconnects architecture. Journal of Micromechanics and Microengineering.31(6),2021.
45. C. Plesa, and C. Dekker, “Data analysis methods for solid-state nanopores,” Nanotechnology, 26 (8), 084003 (2015).
46. J. Larkin, R. Y. Henley, M. Muthukumar, “High-bandwidth protein analysis using solid-state nanopores,” Biophysical journal, 106 (3), 696 –704 (2014).
47. D. Fologea, B. Ledden, D. S. McNabb, “Electrical characterization of protein molecules by a solid-state nanopore,” Applied physics letters, 91 (5), 053901 (2007).
48. H.Asadzadeh and A.Moosavi,” Investigation of the interactions between Melittin and the PLGA and PLA polymers: molecular dynamic simulation and binding free energy calculation,” Material research express, 6(5), 055318,(2019).
49. R. M. Smeets, U. F. Keyser, D. Krapf, “Salt dependence of ion transport and DNA translocation through solid-state nanopores,” Nano letters, 6 (1), 89 –95 (2006).
50. Label-Free Optical Detection of Biomolecular Translocation through Nanopore Arrays
51. U. Keyser, J. Van der Does, C. Dekker, “Optical tweezers for force measurements on DNA in nanopores,” Review of Scientific Instruments, 77 (10), 105105 (2006).
52. H. Asadzadeh, A. Moosavi and JH. Arghavani,” The effect of chitosan and PEG polymers on stabilization of GF-17 structure: A molecular dynamics study,” Carbohydrate polymers,237, 116124 (2020).
53. N. Di Fiori, A. Squires, D. Bar, “Optoelectronic control of surface charge and translocation dynamics in solid-state nanopores,” Nature nanotechnology, 8 (12), 946 (2013).
54. M.Tajedini, A.T. Osmanson, Y. R.Kim, H. Madanipour, C. U. Kim, B. Glasscock, M.Khan,” Electromigration effect on the Pd coated Cu wirebond” IEEE 71st Electronic Components and Technology Conference, 661-666(2021)
55. M. P. Jonsson, and C. Dekker, “Plasmonic nanopore for electrical profiling of optical intensity landscapes,” Nano letters, 13 (3), 1029 –1033 (2013).
56. M.Giesbers, J.M. Kleijn, M.A. Cohen Stuart. The Electrical Double Layer on Gold Probed by Electrokinetic and Surface Force Measurements. Journal of Colloid and Interface Science,248(1),88-95,2002.
57. F. Nicoli, D. Verschueren, M. Klein, “DNA translocations through solid-state plasmonic nanopores,” Nano letters, 14 (12), 6917 –6925 (2014).
58. D. V. Melnikov, Z. K. Hulings, and M. E. Gracheva. Concentration Polarization, Surface Charge, and Ionic Current Blockade in Nanopores. J. Phys. Chem. C , 124, 36, 19802,2020.
59. X. Shi, D. V. Verschueren, and C. Dekker, “Active Delivery of Single DNA Molecules into a Plasmonic Nanopore for Label-Free Optical Sensing,” Nano letters, 18 (12), 8003 –8010 (2018).
60. D. Verschueren, X. Shi, and C. Dekker, “Nano-Optical Tweezing of Single Proteins in Plasmonic Nanopores,” Small Methods, 1800465 (2019).